

## Electronic Properties and Mid-Infrared Transitions in Self-Assembled Quantum Dots

Jean-Pierre LEBURTON<sup>1,2</sup>, Leornaldo R. C. FONSECA<sup>2</sup>, John SHUMWAY<sup>2,3</sup>,  
 David CEPERLEY<sup>2,3</sup> and Richard M. MARTIN<sup>2,3</sup>

<sup>1</sup>Department of Electrical and Computer Engineering, University of Illinois at Urbana-Champaign, Urbana, IL 61801, USA

<sup>2</sup>Beckman Institute of Advanced Science & Technology, University of Illinois at Urbana-Champaign, Urbana, IL 61801, USA

<sup>3</sup>Department of Physics, University of Illinois at Urbana-Champaign, Urbana, IL 61801, USA

(Received June 1, 1998; accepted for publication October 8, 1998)

We present a detailed model of the electronic properties of single and vertically aligned self-assembled pyramidal InAs/GaAs quantum dots (SADs) which is based on the self-consistent solution of three-dimensional (3D) Poisson and Schrödinger equations within the local (spin) density approximation. Nonparabolicity of the band structure and a continuum model for strain between GaAs and InAs results in position and energy dependent effective mass. In single SADs, shell structures obeying Hund's rule for various occupation numbers in the pyramids agree well with recent capacitance measurements. The electronic spectra of SADs of various shapes have been determined with intraband level transitions and mid-infrared optical matrix elements. In the case of two vertically aligned pyramidal SADs, we show that quantum mechanical coupling alone between identical dots underestimates the magnitude of the coupling between the dots, which in large part is due to piezoelectricity and size difference between SADs.

KEYWORDS: nanostructures, quantum dots, shell structures, single-electron charging

### 1. Introduction

Due to their small size, self-assembled quantum dots offer an excellent opportunity to study the physics of highly-confined few-electron systems. Furthermore, possible applications of quantum dot structures such as lasers,<sup>1)</sup> spectral detectors,<sup>2)</sup> and optical memories<sup>3)</sup> have spurred considerable interest in those systems.

Very recent works have demonstrated the electronic shell structure and spin effects in lithographically defined quantum dots containing more than 40 extra electrons.<sup>4)</sup> These “artificial atoms” have shown shell filling with spin ordering predicted by Hund’s rule. In other experiments using small self-assembled quantum dots containing up to 6 extra electrons,<sup>5)</sup> the shell structure in the dots displayed an energy spectrum very different from the simple Coulomb blockade picture observed in metallic and mesoscopic structures. The combination of capacitance and far-infrared spectroscopy in these experiments<sup>5)</sup> has provided experimental information on level separation, as well as on the electron-electron interaction energy of the *s*- and *p*-states within a single InAs-GaAs quantum dot.

In this study, we investigate the quantum mechanical properties and electron-electron interaction within a single quantum dot as well as in vertically coupled quantum dots,<sup>6–8)</sup> using a realistic structure with electron interactions treated within the density functional theory (DFT).<sup>9)</sup> The structures are complete multilayer devices containing one or two pyramidal self-assembled InAs quantum dots embedded in a GaAs matrix (Fig. 1). The number of electrons in the dots is controlled by applying a voltage to a metal gate on top of the device. Strain in the pyramids, wetting layer, and surrounding GaAs matrix is calculated using a continuum model described previously.<sup>9,10)</sup> The bulk electron effective mass and band diagram are considerably modified by the strain in the region of the dots, becoming position dependent. In order to accurately determine the bias voltage at which charging occurs, we use the concept of transition states. We use the local spin density approximation (LSDA) to calculate the many-body interaction<sup>11)</sup> and the energies of possible spin configurations in the

dot showing that the dot filling indeed follows Hund’s rule.

In the case of a stacked InAs/GaAs double-dot system,<sup>6–8)</sup> we calculate level splitting as a function of dot distance. The position of the levels with and without considering strain anisotropy and piezoelectricity shows the contribution to level splitting of each of these effects. In addition, we also consider indium diffusion as well as dots of unequal size and shape.

### 2. Model

In the DFT framework, the three-dimensional Schrödinger equation, written in the envelope function approximation, reads<sup>9)</sup>

$$\left\{ -\frac{\hbar^2}{2} \nabla [M^{-1} \nabla] + V(\mathbf{r}) \right\} \psi_n(\mathbf{r}) = E_n \psi_n(\mathbf{r}), \quad (1)$$

where  $M$  is the electron effective mass tensor and the potential energy  $V$  is given by

$$V(\mathbf{r}) = V_{\text{ext}}(\mathbf{r}) + V_{\text{off}}(\mathbf{r}) + V_c(\mathbf{r}) + V_P(\mathbf{r}), \quad (2)$$

where  $V_{\text{ext}}(\mathbf{r})$  is the potential due to an externally applied voltage,  $V_{\text{off}}(\mathbf{r})$  is the conduction band offset,  $V_c(\mathbf{r})$  is the conduction band strain potential, and  $V_P(\mathbf{r})$  is the piezoelectric potential. Due to strain, the electron effective mass becomes anisotropic leading to a mass tensor given by  $\text{diag}(M) = (m_{xx} m_{yy} m_{zz})$  and zero off-diagonal terms.<sup>12)</sup> In the usual case of sample growth along the crystal direction (001), the electron masses along the plane perpendicular to the growth direction are equal, i.e.  $m_{xx} = m_{yy}$ .

The strain tensor is obtained from the minimization of the elastic energy of the system.<sup>13)</sup> This procedure provides the strain tensor components  $\varepsilon_{xx}$ ,  $\varepsilon_{yy}$ , and  $\varepsilon_{zz}$ , as well as the shear components  $\varepsilon_{xy}$ ,  $\varepsilon_{xz}$ , and  $\varepsilon_{yz}$ . The hydrostatic and biaxial components of the strain, defined as

$$\varepsilon_h(\mathbf{r}) = \varepsilon_{xx}(\mathbf{r}) + \varepsilon_{yy}(\mathbf{r}) + \varepsilon_{zz}(\mathbf{r}) \quad (3)$$

$$\varepsilon_b(\mathbf{r}) = \varepsilon_{xx}(\mathbf{r}) + \varepsilon_{yy}(\mathbf{r}) - 2\varepsilon_{zz}(\mathbf{r}), \quad (4)$$

respectively, play a major role in the electronic structure of the dot. Ignoring the split-off bands, one can derive the band-

edge energies at the Brillouin zone center ( $\mathbf{k} = 0$ ):<sup>14)</sup>

$$\begin{aligned} V_c(\mathbf{r}) &= E_g + a_c \varepsilon_h(\mathbf{r}) \\ V_{\text{hh}}(\mathbf{r}) &= a_v \varepsilon_h(\mathbf{r}) + \frac{b}{2} \varepsilon_b(\mathbf{r}) \\ V_{\text{lh}}(\mathbf{r}) &= a_v \varepsilon_h(\mathbf{r}) - \frac{b}{2} \varepsilon_b(\mathbf{r}), \end{aligned} \quad (5)$$

where  $E_g$  is the unstrained band gap energy, and  $V_{\text{hh}}$  and  $V_{\text{lh}}$  are the heavy hole and light hole bands. The deformation potentials  $a_c$ ,  $a_v$ , and  $b$  for InAs and GaAs are given in ref. 9.

The presence of the shear strains in the InAs-GaAs interfaces leads to the appearance of a polarization charge and its associated piezoelectric potential which reduce the symmetry of the system, lifting some of the degeneracies calculated for unstrained pyramidal quantum dot systems. Piezoelectric effects in single dots of realistic sizes are very small, changing the eigenvalues of the system by less than 1 meV, and can be neglected.<sup>15)</sup> However, they may be considerably larger in systems of closely spaced dots since their amplitude is different in each dot (see §3). The piezoelectric polarization  $\mathbf{P}$  and associated piezoelectric polarization charge  $\rho_P$  are defined as<sup>15)</sup>

$$\rho_P = \nabla \cdot \mathbf{P}, \quad P_i = \sum_{i,j} e_{ijk} \varepsilon_{jk}, \quad i, j, k = x, y, z, \quad (6)$$

where  $e_{ijk}$  denotes the piezoelectric constants,  $e_{123} = e_{231} = e_{312}$ . The piezoelectric potential  $V_P$  is the solution of the Poisson equation

$$\nabla^2 V_P = -\frac{q}{\varepsilon(\mathbf{r})} \rho_P(\mathbf{r}). \quad (7)$$

Using time-independent perturbation theory up to the second order, we obtain the following expressions for the diagonal components of electron effective mass tensor:<sup>9)</sup>

$$\begin{aligned} m_z^*(E_i, \mathbf{r}) &= m^*(V_c(\mathbf{r}) - V_{\text{lh}}(\mathbf{r}))/E'_g \\ m_{x,y}^*(E_i, \mathbf{r}) &= m^*(V_c(\mathbf{r}) - V_{\text{hh}}(\mathbf{r}))(V_c(\mathbf{r}) - V_{\text{lh}}(\mathbf{r})) \\ &\quad / [E'_g(V_c - 0.75V_{\text{lh}}(\mathbf{r}) - 0.25V_{\text{hh}}(\mathbf{r}))], \end{aligned} \quad (8)$$

where  $E'_g = E_g + E_i$ ,  $E_i$  is the  $i$ th eigenvalue, and  $m^*(E_i, \mathbf{r})$ ,  $m_z^*(E_i, \mathbf{r})$ , and  $m_{x,y}^*(E_i, \mathbf{r})$  denote bulk, perpendicular, and in-plane electron effective masses (the wetting layer lies in the  $xy$  plane) of an electron with associated eigenvalue  $E_i$ . The remaining components of the effective mass tensor are zero. The presence of the eigenenergy  $E_i$  in eq. (8) is for the correction of a large separation between the eigenstates and the conduction band edge. A detailed derivation of eq. (8) including a comparison with an 8-band  $\mathbf{k} \cdot \mathbf{p}$  calculation can be found elsewhere.<sup>16)</sup>

The Schrödinger equation is solved using the iterative extraction-orthogonalization method (IEOM).<sup>17)</sup> The major advantage of IEOM is its efficiency resulting from its ability to generate an arbitrarily small number of eigenstates  $N_E$ . As a result, the method scales as  $N_E^2 N_G$ , i.e., is linear in  $N_G$ . Unfortunately, the convergence of IEOM also scales with the inverse of the separation between eigenvalues, which can be very small for near degeneracies typical in weakly coupled quantum dot systems. In order to improve convergence in the coupled quantum dot system, we have implemented an inverse iteration scheme which uses the approximate eigenvalues of IEOM as a guess  $E_{\text{guess}}$  for the eigenvalues:<sup>12)</sup>

$$(H - E_{\text{guess}})\psi^i = \psi^{i-1}, \quad (9)$$

where  $H$  is the Hamiltonian and the index  $i$  refers to the iteration number. One problem with inverse iteration is that it converges to the eigenstate corresponding to the eigenvalue closest to  $E_{\text{guess}}$ . To avoid missing states, we use  $E_{\text{guess}}$  lower than the eigenvalue corresponding to the eigenstate to which the system is converging, and we orthogonalize the states after each iteration. A biconjugate gradient scheme is used to solve eq. (9).

## 2.1 Local spin density approximation

The quantum mechanical correction of many-electron interactions in the context of device physics is calculated using the LSDA of the Kohn-Sham DFT.<sup>18)</sup> In this approximation, the exchange-correlation energy  $E_{xc}[n^\alpha, n^\beta]$  is a function of the  $\alpha$ -electron and  $\beta$ -electron densities  $n^\alpha(\mathbf{r})$  and  $n^\beta(\mathbf{r})$ , where  $\alpha$  and  $\beta$  denote up and down spins, respectively. The exchange term becomes not only a function of the total charge density  $n = n_\uparrow + n_\downarrow$  but also a function of the polarization parameter  $\zeta$ ,

$$\zeta = -\frac{n^\uparrow - n^\downarrow}{n}. \quad (10)$$

## 2.2 Transition state

The Kohn-Sham eqs. (1) and (2) only provide the ground state of the system and its total energy  $E_T$ . A rigorous way of determining the number of electrons  $N$  in a quantum dot with the electron charge as a good quantum number is to minimize  $E_T(N)$ , for  $N = 1, 2, \dots, N_{\max}$ . This minimization should be repeated whenever the external voltage bias  $V_g$  is changed. The use of only eigenvalues to determine the charge in the dot, where charging occurs whenever an eigenvalue crosses the Fermi level, is only correct in the limit of weakly interacting electron systems.

However, the Kohn-Sham theory is not restricted to integer numbers of electrons in the system. Differentiating  $E_T$  with respect to the noninteger occupation number  $n_i$  of level  $i$  one obtains

$$\frac{\partial E_T}{\partial n_i} = \varepsilon_i. \quad (11)$$

Equation (11), the Janak theorem,<sup>19)</sup> provides a meaning to the eigenvalues of the Kohn-Sham equation. Integrating eq. (11) between  $N$  and  $N+1$  one obtains the so-called Slater formula:<sup>20)</sup>

$$E_T(N+1) - E_T(N) = \int_0^1 \varepsilon_{LAO}(n) dn \approx \varepsilon_{LAO} \left( \frac{1}{2} \right), \quad (12)$$

where  $\varepsilon_{LAO}$  corresponds the eigenvalue of the lowest available orbital. The last step in eq. (12) is exact if  $\varepsilon_{LAO}$  is a linear function of the occupation number. In order to determine if there are  $N$  or  $N+1$  electrons in the dot, one defines the transition state as the state containing  $N+0.5$  electrons. If  $\varepsilon(1/2)$  is positive then  $E_T(N+1) > E_T(N)$  and the dot contains  $N$  electrons, otherwise it contains  $N+1$  electrons.<sup>9)</sup>

## 3. Results

Figure 1(a) shows a single quantum dot device which consists of a highly doped ( $10^{18}/\text{cm}^3$ ) 420 Å GaAs substrate, fol-

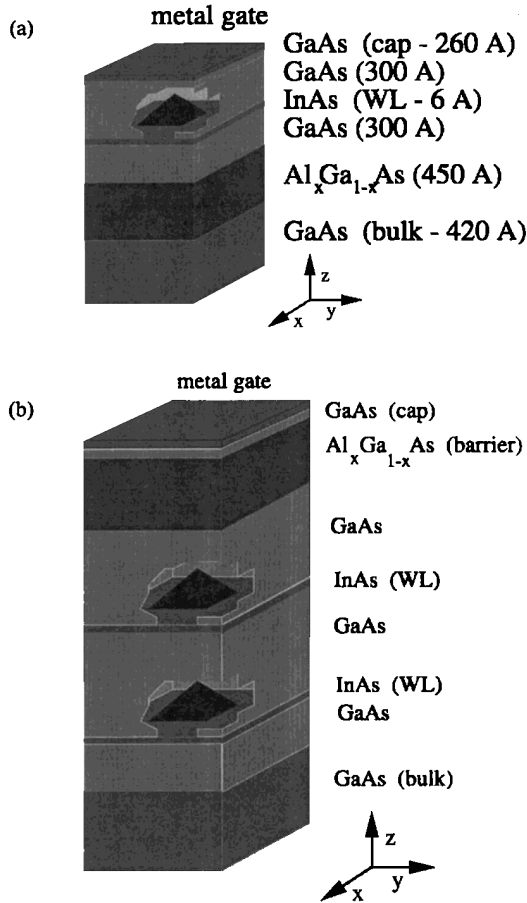


Fig. 1. Schematic representation of the self-assembled (a) quantum dot and (b) stacked double dot structures used in the present work.

lowed by a 450 Å Al<sub>0.3</sub>Ga<sub>0.7</sub>As barrier layer. The active region consists of two 300 Å-wide layers of undoped GaAs surrounding a 6 Å InAs wetting layer and a InAs pyramid. A highly doped ( $10^{18}/\text{cm}^3$ ) 260 Å GaAs cap and a metallic gate complete the device. We have assumed a conduction band offset  $\Delta E_c = 770 \text{ meV}$  between bulk GaAs and bulk InAs (ratio  $\Delta E_c/\Delta E_g = 70\%$ ), and bulk electron effective masses in GaAs and InAs of  $0.067m_e$  and  $0.023m_e$ ,<sup>14)</sup> respectively, where  $m_e$  is the bare electron mass. As described below, these effective masses and the conduction band offset change considerably as strain is considered in the calculation (the calculation of strain is indispensable for an accurate simulation of the InAs-GaAs heterostructure due to its rather large lattice mismatch, of the order of 7%). All the calculations were performed at 4.2 K.

Figures 2(a) and 2(b) show the strain potential and electron effective masses along the  $z$  direction, through the tip of the pyramid. Notice the large value of the strain potential which reduces the conduction band offset between the two materials, and the considerable modification of the bulk effective mass, by a factor of two in average, which is in good agreement with the work of Cusack *et al.*<sup>21)</sup> The spikes near the tip of the pyramid have a numeric origin, and are caused by the difficulty in calculating the strain components around the edges of the pyramid. The presence of the shear strains in the InAs-GaAs interfaces leads to the appearance of a polarization charge and its associated piezoelectric potential, which reduces the symmetry of the system, lifting some of the de-

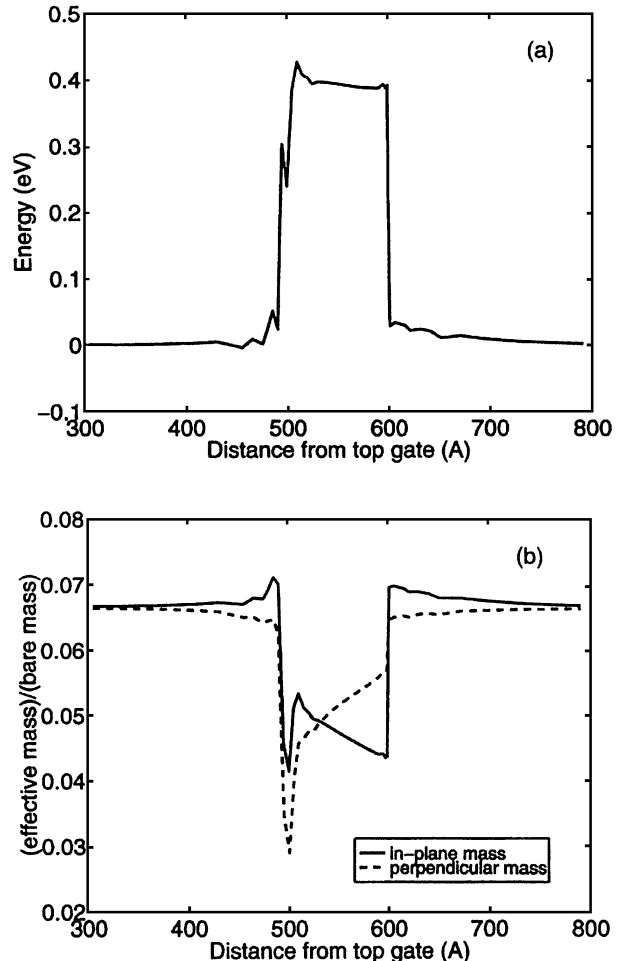


Fig. 2. (a) Strain potential; (b) perpendicular and in-plane electron effective masses along  $z$  direction through the tip of the pyramid (in units of bare electron mass). The pyramid base size is 200 Å and the height is 100 Å.

generacies observed in pyramidal quantum dot systems.

Figure 3 shows the first ten eigenvalues of empty dots as a function of dot base length (also called base diameter), keeping the wetting layer width fixed. The eigen-values were calculated with respect to the average conduction band edge position in the barrier. Figure 3 also shows the approximate depth of the well and the energy difference between the first ( $0\ 0\ 0$ ) and second ( $1\ 0\ 0$ ) states, and between the second and third ( $0\ 0\ 1$ ) states. The notation  $(n_i n_j n_k)$  corresponds to the number of nodes of the eigenfunction in the  $x$ ,  $y$ , and  $z$  directions, respectively. The eigenvalues were only calculated while the states remained bound or quasibound. As the eigenvalues approach the top of the well, the slopes of the curves tend to decrease, as a result of deeper wave function penetration in the barrier region. For energies above the well height, the corresponding eigenfunctions spread over the wetting layer, becoming a 2-dimensional electron gas.

Neglecting piezoelectric effect, the Hamiltonian of the quantum dot is invariant under the symmetry operations of the group  $C_{4v}$ ,<sup>22)</sup> which allows the wave functions to be symmetrized according to the irreducible representations of this group. It can be easily verified that only  $p$ -like states (such as  $(1\ 0\ 0)$ ) can be degenerate, while all other degeneracies are accidental. That explains why the states  $(2\ 0\ 0)$  and  $(0\ 2$

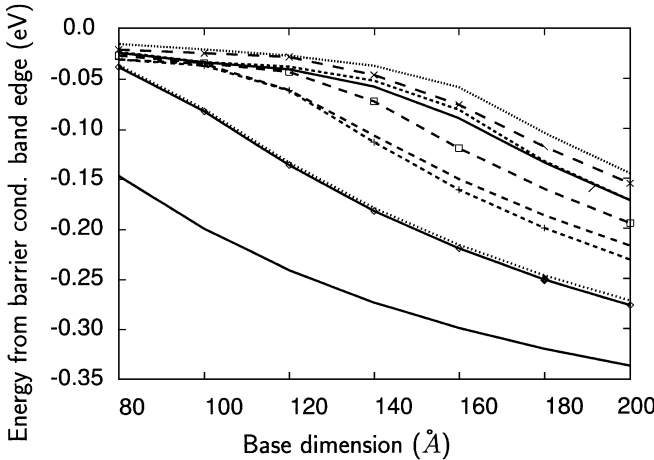


Fig. 3. Approximate well depth (thick solid line) and eigenvalues of the Hamiltonian as a function of dot diameter  $d$ . The eigenvalues were calculated with respect to the average conduction band edge in the region of the pyramid. States represented, from low to high energy:  $(0\ 0\ 0)$ ,  $(1\ 0\ 0)/(0\ 1\ 0)$ ,  $(0\ 0\ 1)$ ,  $(1\ 1\ 0)$ ,  $(2\ 0\ 0)+(0\ 2\ 0)$ ,  $(2\ 0\ 0)-(0\ 2\ 0)$ ,  $(1\ 0\ 1)/(0\ 1\ 1)$ , and  $(1\ 1\ 1)$ . The notation  $(n_1 n_2 n_3)$  denotes the number of wave function nodes in the  $x$ ,  $y$ , and  $z$  directions. Degenerate states are separated by a slash. Pyramid height  $h = d/2$ . Lines are guides for the eye.

0) are not degenerate in a finite barrier pyramid, even though they are degenerate in a square well. In the last case, degeneracy occurs because the Hamiltonian allows the separation of variables. One can also show that the irreducible representation of those two states are the linear combinations  $(2\ 0\ 0)+(0\ 2\ 0)$  and  $(2\ 0\ 0)-(0\ 2\ 0)$ , shown as the fifth and sixth curves from bottom to the top of Fig. 3 (solid line with stars and dashed line with crosses, respectively). Perhaps this counterintuitive result can be more easily understood with the help of Fig. 4. It shows that the projections of the states  $(2\ 0\ 0)+(0\ 2\ 0)$  and  $(2\ 0\ 0)-(0\ 2\ 0)$  are very different, thus are affected differently by the pyramidal confining potential.<sup>9)</sup> As a result, the energies of the two states do not need to be the same. Our calculations agree well with those of ref. 21 in the range of sizes investigated in that work. As discussed in §2, these eigenvalues may change considerably if a full 8-band  $\mathbf{k} \cdot \mathbf{p}$  calculation is performed.<sup>16)</sup>

The quantum dot shape can sometimes be controlled during the experiment but, particularly in the case of self assembled dots, the shape is a result of the growth process and must be measured. Scanning tunneling microscopy (STM) and atomic force microscopy (AFM),<sup>23)</sup> have shown that dots can grow as faceted pyramids or with rounded lens shapes. The shape is dependent on the growth process and shape transitions have been observed.<sup>23)</sup> The reduced symmetry of square dots causes degeneracy splitting, so that infrared absorption and photoconductivity experiments may distinguish between lens-like and pyramidal dots.

While atoms are characterized by three-dimensional rotational symmetry, leading to the quantization of angular momentum and description in terms of the  $l$  and  $m_l$  quantum numbers, or equivalently the notation  $s$ ,  $p$ ,  $d$ ,  $f \dots$ , quantum dots have reduced symmetry and should not be labeled in this manner. Nevertheless, we will adopt the notation  $1s$ ,  $2p_x$ ,  $2p_y$ ,  $3d_{xy}$ ,  $3p_x$ ,  $3d_{x^2-y^2}$ , and  $2s$  describes the six lowest states so that our results may be compared to those

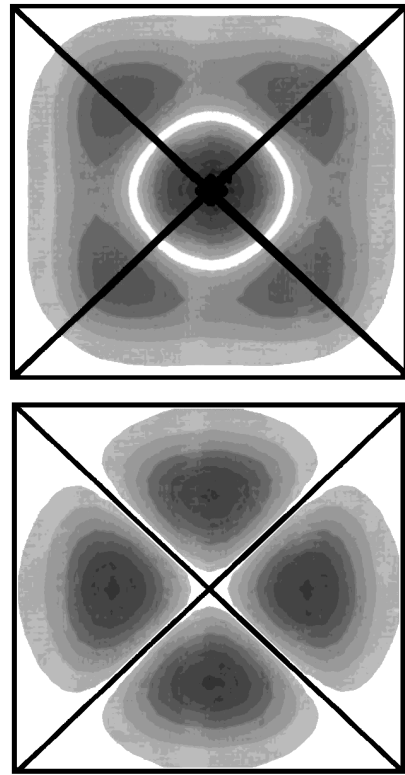


Fig. 4. Projections of the states  $(2\ 0\ 0)+(0\ 2\ 0)$  (top) and  $(2\ 0\ 0)-(0\ 2\ 0)$  (bottom). Notice the lobes of the top state along the diagonals (crossed lines) of the base of the pyramid (square box), lowering its energy with respect to the more confined bottom state.

in existing literature and as an aid in comparisons between lens-like and pyramidal symmetry. In effect, the states in a lens should be labeled by the irreducible representations of the  $C_\infty$  group:<sup>24)</sup>  $1a_1(1s)$ ,  $1e_1(2p_x, 2p_y)$ ,  $1e_2(3d_{xy}, 3d_{x^2-y^2})$ , and  $2a_1(2s)$ , where the expressions in parenthesis are the notations used by us. As mentioned before, for a pyramid the symmetry group is  $C_4$ , and proper labeling is  $1a_1(1s)$ ,  $1e_1(2p_x, 2p_y)$ ,  $1b_2(3d_{xy}, 3d_{x^2-y^2})$ , and  $2a_1(2s)$ . The effect of symmetry reduction from a lens to a pyramid is to break the degeneracy of the  $d$ -states, leading to a lower energy state  $3d_{xy}$  with lobes in the corners of the confining potential, and a higher energy state  $3d_{x^2-y^2}$  with nodes in the corners of the potential. The degeneracy in states with odd values of angular momentum is unaffected by a reduction to pyramidal symmetry. One weakness of our adopted notation is that the  $2s$  state actually contains a linear combination of atomic-like  $2s$  and  $2p_z$  states, an effect which shows up in the  $z$ -polarized dipole selection rules.

Figure 5 shows the comparison of the lowest single particle eigenstates for lens and pyramidal dots, as well as a couple of simple theoretical models: a hard wall rectangular box and a parabolic potential. The box and parabolic potential exhibit an accidental degeneracy, due to the separability of the  $x$ ,  $y$ , and  $z$  degrees of freedom in the single particle Schrödinger equation for these potentials. The box and parabolic wave functions are often represented by the three quantum numbers  $(n_i, n_j, n_k)$ . States  $(1, 0, 0)$  and  $(0, 1, 0)$  are degenerate, as are  $(2, 0, 0)$  and  $(0, 2, 0)$ . The  $(1, 0, 0)$ ,  $(0, 1, 0)$  pair corresponds to the  $(2p_x, 2p_x)$  degenerate pair present in both the square and circular symmetry, but the  $(2, 0, 0)$ ,  $(0, 2, 0)$  pair must be re-

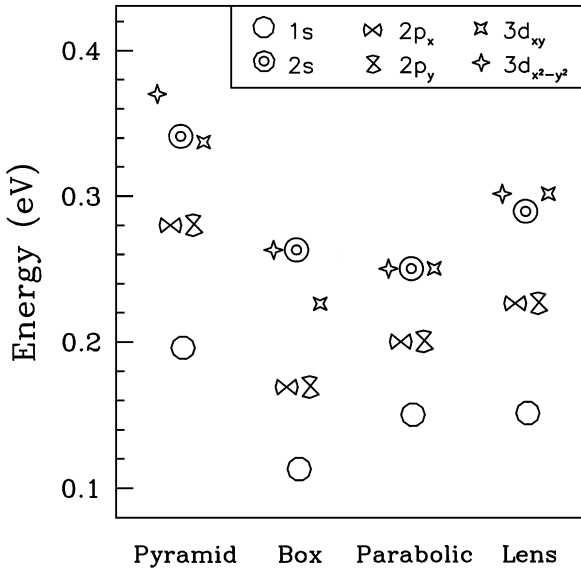


Fig. 5. The single particle energies of different shaped potentials for  $200 \times 200 \times 100 \text{ \AA}^3$  dots with  $m_e = 0.05$ . The round lens  $D = 200 \text{ \AA}$   $h = 100 \text{ \AA}$  and parabolic ( $w_x = w_y = 0.25w_z - m \text{ eV}$ ) dots have degenerate  $d$ -states, and the reduced symmetry of the pyramid and box cause the  $3d_{xy}$  state to lie below the  $3d_{x^2-y^2}$  state. The separable potentials for the box and parabolic potentials have an additional degeneracy between the  $2s$  and  $3d_{x^2-y^2}$  states, which is lifted by interactions.<sup>9)</sup>

combined to get the  $3d_{x^2-y^2} = [(2, 0, 0) - (0, 2, 0)]/\sqrt{2}$  and  $2s = [(2, 0, 0) - (0, 2, 0)]/\sqrt{2}$  states. Thus these separable potentials contain an accidental degeneracy between the  $3d_{x^2-y^2}$  and  $2s$  states that is lifted by a slight change in the confining potential or the introduction of interactions.<sup>9)</sup>

The selection rules for dipole-allowed transitions are determined by the requirement that  $\langle \Psi_i | \mathbf{r} \cdot \hat{\mathbf{e}} | \Psi_f \rangle$  be nonzero, where  $\hat{\mathbf{e}}$  is the electron polarization operator, and  $\Psi_i$  and  $\Psi_f$  are the many-body initial and final states, respectively. For circular symmetry, the allowed transitions are  $\Delta l_z = \pm 1$  for  $x, y$  polarization and  $\Delta l_z = 0$  for  $z$  polarization. In the case of square symmetry, group theory gives the rules as  $e \leftrightarrow \{a_1, a_2, b_1, b_2\}$  because  $x, y$  polarization and  $z$ -dipole transitions only occur between states of the same symmetry. In the case of charged quantum dots, the same transition rules for both shapes,  $x, y$  transitions  $2p_{xy} \leftrightarrow \{1s, 3d_{xy}, 3d_{x^2-y^2}, 2s\}$  and one allowed  $z$  transition,  $1s \leftrightarrow 2s$ , exist.

We show calculated infrared absorption spectra for a pyramidal dot in Fig. 6. Hartree energy shifts the energy of the  $1s$  state more than other states, since this state sits in the center of the dot. The result is that the  $1s \leftrightarrow 2p_{x,y}$  transition overlaps the energy of the transitions from the  $2p_{x,y}$  states.<sup>25)</sup> This can give the appearance of a single transition, when in fact, several transitions contribute to a spectral line. Also, it would be possible to incorrectly associate these evenly spaced transitions in this pyramidal dot as indicative of a parabolic confining potential. The prominent split of the energy for the transitions to the  $3d_{xy}$  and  $3d_{x^2-y^2}$  states in our calculations show the breaking of the axial symmetry in the dot.

Figure 7 shows the number of electrons in a  $200 \text{ \AA}$  base diameter and  $70 \text{ \AA}$  height pyramidal quantum dot as a function of gate voltage  $V_g$ . Two curves are shown, corresponding to charging sequences which obey and disobey Hund's rule. When Hund's rule is obeyed it means that the charging of the

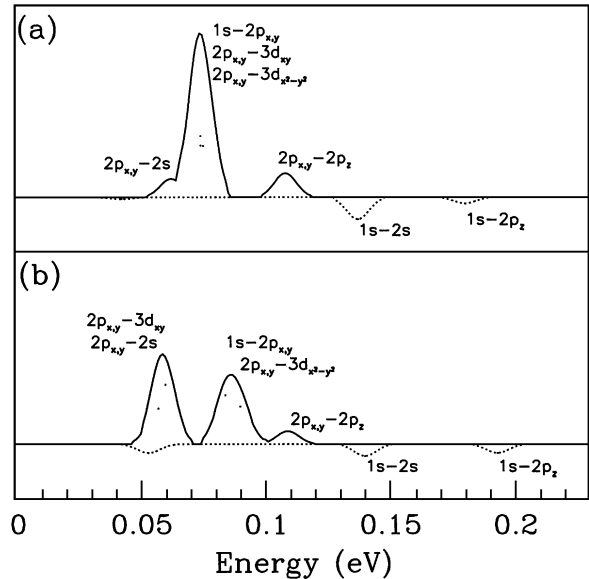


Fig. 6. Computed dipole matrix elements for transitions between different states for lens- (a) and pyramidal-shape (b) quantum dots. Transitions from  $3d$ -states up have not been considered.

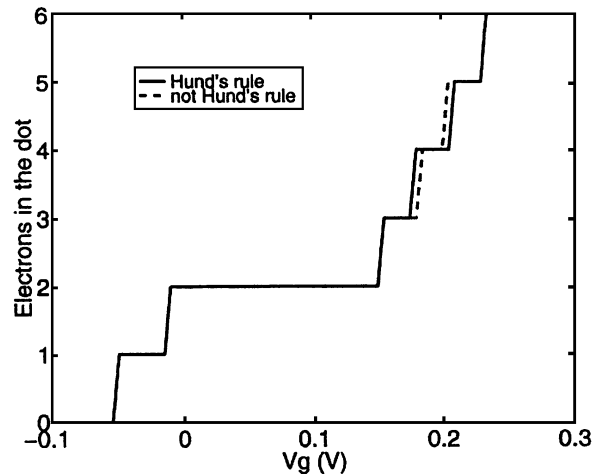


Fig. 7. Number of electrons in the dot as a function of gate voltage  $V_g$  in the case of obeying Hund's rule (second level population following the spin sequence  $2p_x^\uparrow 2p_y^\uparrow 2p_x^\downarrow 2p_y^\downarrow$ ), and disobeying Hund's rule (second level spin sequence  $2p_x^\uparrow 2p_y^\downarrow 2p_x^\downarrow 2p_y^\uparrow$ ). The dotted curve coincides with the solid curve whenever the dots are not visible. Pyramid base size=  $200 \text{ \AA}$  and height=  $70 \text{ \AA}$ .

four-fold degenerate second level follows the spin sequence  $2p_x^\uparrow 2p_y^\uparrow 2p_x^\downarrow 2p_y^\downarrow$ . The curve that does not follow Hund's rule was obtained by charging the second level according to the spin sequence  $2p_x^\uparrow 2p_y^\downarrow 2p_x^\uparrow 2p_y^\downarrow$ . The third possibility, namely the spin sequence  $2p_x^\uparrow 2p_x^\downarrow 2p_y^\uparrow 2p_y^\downarrow$ , was not considered because it will clearly be unfavorable due to the intense coulomb repulsion between the  $2p_x^\uparrow$  and the  $2p_x^\downarrow$  electrons resulting from their large wave function overlap. The step size obtained with LSDA corresponding to the charging of the fourth electron ( $N = 3$ ) is longer for the charging of the dot according to the spin sequence  $1s^\uparrow 1s^\downarrow 2p_x^\uparrow 2p_y^\downarrow$  than for  $1s^\uparrow 1s^\downarrow 2p_x^\uparrow 2p_y^\uparrow$ , indicating that indeed Hund's rule is followed by this system. The electron-electron interaction energy difference between the two spin configurations for four electrons in the dot is

$\sim 3$  meV.

The addition of the fourth electron following Hund's rule is less costly because of the presence of exchange interaction (attractive) in this case but not if the spin of the fourth electron is different from the spin of the third. Analogously, the step corresponding to the charging of the fifth electron ( $N = 4$ ) is shorter for the sequence  $2p_x^{\uparrow}2p_y^{\downarrow}2p_x^{\uparrow}2p_y^{\downarrow}$  because the fifth electron, either in the  $2p_x^{\uparrow}$  or  $2p_y^{\downarrow}$  state, interacts by exchange with one of the two electrons already in the second level, while according to Hund's rule, the fifth electron does not interact by exchange with any of the other two because of their different spin states.

We have estimated pairwise electron-electron interaction energies. Table I summarizes and compares those results with the values inferred from the capacitance data by Fricke *et al.*<sup>5)</sup> Differences between energies obtained from calculations and inferred from measurements may result from our assumption that the different types of interaction ( $s - s$ ,  $p - s$ , or  $p - p$ ) remain unchanged as more electrons are added to the dot. A second source of error in our calculation is the exclusion of interdot repulsion, which should push the electrons closer together inside the dot. However, as we have already pointed, for dot densities of  $10^{10}/\text{cm}^2$ , the inclusion of interdot effects should change our results by less than 1 meV by pushing the electrons in the dot closer together. Finally, the approximation used to calculate the hartree energy may lead to some correction in our calculation. As far as the analysis of the experimental data is concerned,<sup>5)</sup> it included the image charge effect but excluded interdot repulsion. In fact, these two competing effects nearly cancel each other for dot densities in the range of  $1-10 \times 10^{10}/\text{cm}^2$ . The analysis of the experimental data also excluded the presence of a charged interface between the gates (the layer of dots charged with one electron each). Indeed, the presence of the layer of charged dots between the gates decreases the electron-electron interaction energy by  $\sim \gamma_{\text{dot}} \times 3$  meV, where  $\rho_{\text{dot}} = \gamma_{\text{dot}} \times 10^{10}/\text{cm}^2$  is the density of dots in the plane. Because this correction is considerably large and linear on  $\gamma_{\text{dot}}$ , it is clear that the extraction of the electron-electron energy from the experimental data requires precise knowledge of the dot density.

The local density approximation DFT, has been widely used to calculate the electron-electron interaction in dots<sup>9,12,17,26-29)</sup> because of its simple implementation and negligible demand for computer time. However, LSDA is an approximate theory well known for high-accuracy calculations as well as wrong predictions of the physical properties of some systems.<sup>30)</sup> In particular, the experience with LSDA on atoms and molecules may not carry over to quantum dots since the confining potentials and electron densities can be very different. In Fig. 8, we compare the results obtained with LSDA in self-assembled quantum dots against those obtained with the diffusion quantum Monte Carlo (DMC) method,

which provides an exact treatment of the many-body interactions.<sup>31)</sup> Figure 8 shows the values of the different components of the total energy as a function of dot occupation. Differences between LSDA and QMC are not apparent on the scale of the figure. This figure clearly shows that the external potential energy and kinetic energy are much larger than the interactions. In other words the interactions may enter as a perturbative effect from the noninteracting system. The reason for this can be seen from the scaled electron density. Then energy and length scales for the electron interaction are scaled by the dielectric and mass, so that the effective Bohr radius is  $a_0^* = \varepsilon/m^*a_0 \approx 150 \text{ \AA}$  and the effective Hartree energy is  $Ha^* = \varepsilon^{-2}m \times Ha \approx 7 \text{ meV}$ . If we approximate the electrons as uniformly occupying the interior of the dot, we obtain an effective electron density of  $r_s \approx 0.46N^{-1/3}$ , which is rather high. In fact, the electron gas has a well-known ground state energy expansion for small  $r_s$ <sup>32)</sup>

$$E = 2.2099r_s^{-2} - 0.9163r_s^{-1} - 0.094 + 0.0622\ln(r_s) + \dots \quad (13)$$

where the first term is the kinetic energy, the second term is the exchange, and the remaining terms refer to correlation energy. For the case of six electrons in the dot  $r_s \approx 0.25$  and the expansion gives  $E_k = 1440 \text{ meV}$ ,  $E_x = 151 \text{ meV}$ , and  $E_c = 0.6 \text{ meV}$ . Although the comparison between these very different electronic systems cannot be stretched too far, this does show that our energy scales are reasonable for a highly effective electron density. The leading effect of the interaction is the Hartree energy, with small corrections for exchange and very small correlation corrections.

Figure 1(b) shows the double quantum dot structures which consist of two pyramidal shaped InAs quantum dots and their corresponding wetting layers embedded in a GaAs matrix. The base lengths and heights of the dots are variable. The material layers, from top to bottom, are: a metal gate, 50 Å GaAs, 300 Å Al<sub>0.3</sub>Ga<sub>0.7</sub>As barrier, 210 Å GaAs with the first 60 Å eight pyramid embedded, a 6 Å wetting layer, a GaAs barrier of variable thickness with the second 60 Å height pyramid embedded, a second 6 Å wetting layer, and a 200 Å GaAs

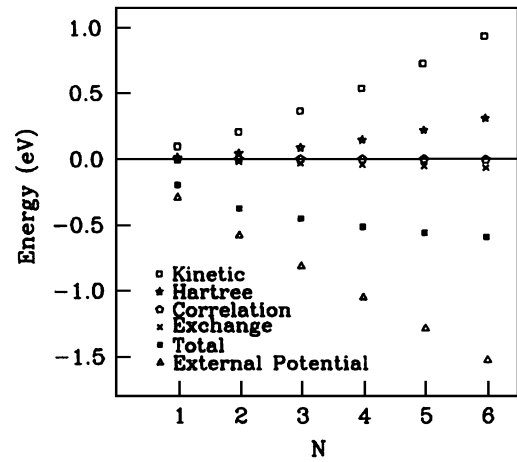


Fig. 8. Contributions to the energy of a  $200 \times 200 \times 100 \text{ \AA}^3$  pyramidal dot as a function of occupation  $N$ , calculated by both LSDA and QMC. Differences between LSDA and QMC are not apparent on the energy scale considered in this figure. This clearly shows the small effect of interactions beyond the Hartree (mean field) level.

Table I. Charging energy per electron pair (in meV) in single SAD.

Interaction type	Calculated	Measured
$s - s$	22	$\sim 23$
$s - p$	$\sim 15$	$\sim 7$
$p - p$	$\sim 13$	$\sim 18$

buffer region. This sequence of materials is similar to what one would find in typical experiments.<sup>33)</sup> However, the highly doped GaAs substrate that would follow the last epitaxial layer in some experiments has been replaced in our simulations by a grounded metal gate.

Figure 9 shows a contour plot of the strain distribution around the two pyramids. Despite the obvious strain potential anisotropy in the GaAs surrounding the dots, the value of the strain potential in those regions is small ( $\ll 10$  meV), as indicated by the values of the isosurfaces. Inside the pyramids, where the strain potential attains significant values, the differences in the strain potential distribution of the two dots becomes almost insignificant. Therefore, one should not expect the strain potential to produce any unexpected features from a calculation only involving a constant shift (of the magnitude of the average shift obtained from the exact strain calculation) of the conduction band edge in the region of the dots and wetting layers. However, the same cannot be said with respect to the piezoelectric potential. Figure 10 shows all the points in space where the piezoelectric potential is greater than 50% of its maximum for both isolated and double dots, corresponding to  $\approx 50$  meV and  $\approx 70$  meV for the isolated and double dots, respectively. The lobes in Fig. 10(b) are bigger than those in Fig. 10(a) because the piezoelectric potentials generated by the stacked dots add up in the regions above and below the two dots. Shades of gray correspond to different signs of the potential. As discussed by Grundmann *et al.*<sup>15)</sup> concerning isolated pyramids, piezoelectric charge, accumulates mostly along the pyramid edges, excluding the edges of the square base (due to the presence of the wetting layer). Charge of different signs accumulates in the inside and outside of the pyramids generating four outer potential lobes along the diagonal edges, as well as four smaller lobes parallel to the edges of the square basis. The signs of the smaller potential lobes are rotated by 90° from the bigger lobes (Fig. 10(a)). However, in the double dot system (Fig. 10(b)) the piezoelectricity is a lot more intense around the top pyramid than around the bottom one due to the near cancellation of the piezoelectric charge accumulated between the dots. Indeed, in closely spaced stacked dots the four smaller lobes from the upper pyramid

appearing on the edges of the square bases nearly cancel out the four bigger lobes along the diagonal edges of the lower pyramid, resulting in the eight lobes displayed in Fig. 10(b). Thus, the piezoelectric potential along the diagonal edges of the lower pyramid is smaller than along the diagonal edges of the upper pyramid and is not visible in Fig. 10(b) due to the particular value of the energy cutoff used in this figure. In addition, the lobes add up in the regions above and below the two dots, enhancing the piezoelectric effects in those regions. The piezoelectric anisotropy leads to nonidentical confining potentials which, as we shall see, strongly influence level splitting.

Figure 11 shows the position of the bound levels of the coupled dot system as a function of dot separation (tip-to-base). In this figure, we do not consider the strain field in detail but just shift the conduction band edge in the pyramids and wetting layers by 400 meV, which is comparable to the shift caused by the exact strain as shown in Fig. 9. By only shifting the InAs conduction band edge, we wish to avoid the effects of strain anisotropy, allowing us to identify the different sources of level splitting. The triplets in parenthesis refer to the number of wave function nodes in each spatial direction ( $xy$ -plane parallel to the wetting layers—see Fig. 1). Actually, the shapes of the wave functions are difficult to de-

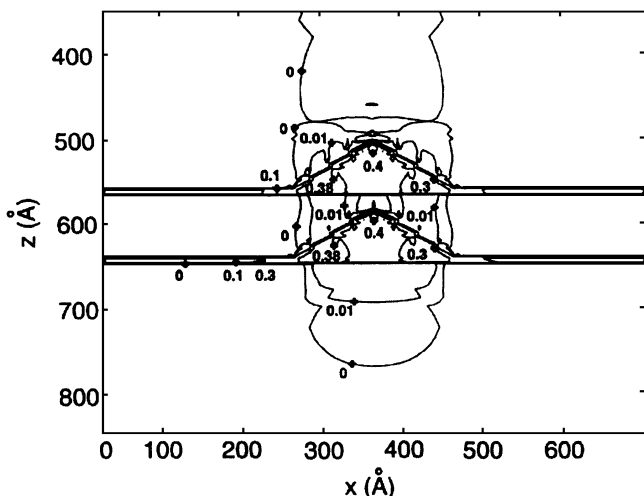


Fig. 9. Contour plot of the strain potential for the stacked double quantum dot structure. The indicated magnitudes of the isosurfaces are in eV. Dot separation is 15 Å.

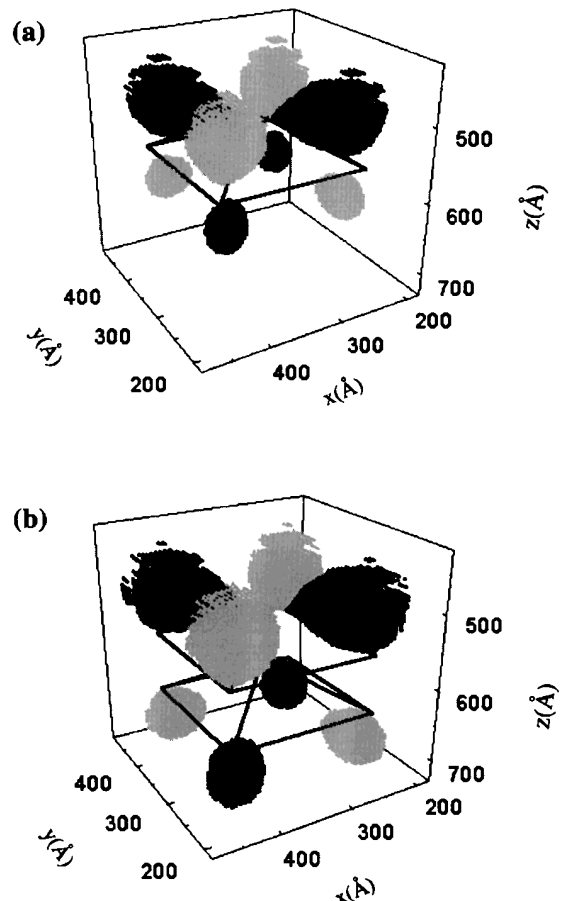


Fig. 10. Piezoelectric potential distribution of points at a potential greater than 50% of the maximum, corresponding to (a)  $\sim 50$  meV in the isolated dot, (b)  $\sim 70$  meV in the double dot system. Black and gray spots correspond to negative and positive potentials, respectively. Dot separation is 15 Å.

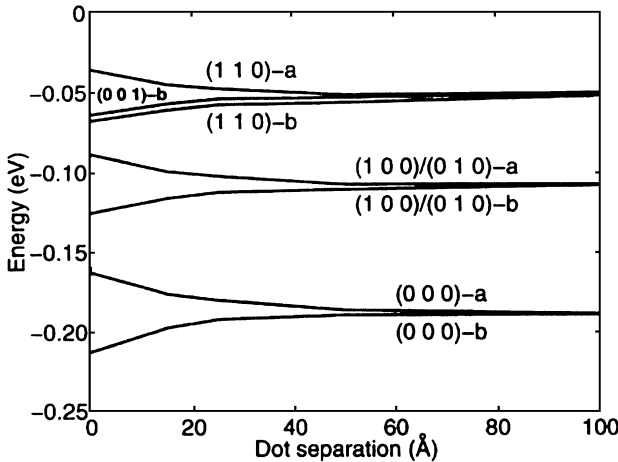


Fig. 11. Eigenenergies as a function of dot separation assuming a constant shift of the conduction band edge of 400 meV in the region of the pyramids and wetting layers. Indium diffusion was not considered.

scribe in terms of the number of nodes, except for the first and second pairs of levels in Fig. 11, which closely resemble *s* and *p* states, respectively. In order to observe level splitting experimentally, it is necessary that the level separation is bigger than 2–3 meV's because of the inhomogeneous broadening resulting from size fluctuations. Thus, Fig. 11 shows that only for separations less than 50 Å sizable level separations would be observed. It should be pointed out that a level crossing occurs between the states  $2p_z - b = (001) - b$  and  $3d_{xy} - a = (110) - a$  for a separation  $\approx 50$  Å, where  $-b$  and  $-a$  refer to bonding and antibonding states, respectively, even though it is hardly visible in Fig. 11. An indication that such a crossing is possible is that those two states do not share the same irreducible representation of the quantum dot *z*-axis symmetry group  $C_{4v}$ .

When piezoelectricity is considered as well as the exact strain field, the changes in all the levels are marked (except for the 1s state) as shown in Fig. 12. The reason for this is the reduction of the *z*-axis symmetry from  $C_{4v}$  to  $C_{2v}$  leading to a level splitting between the  $2p_x = (100)$  and  $2p_y = (010)$  states in each dot. Not only do the  $2p$  states split, the splitting is not the same for the bonding and antibonding states due to the anisotropy of the piezoelectric potential, as shown in Fig. 10. We can therefore conclude that level splitting in stacked quantum dots is mostly influenced by piezoelectricity.

A second major cause of level splitting comes from the possibly different geometries of the dots within the same stack. A common cause for such geometric differences is anisotropic indium diffusion resulting from different indium diffusion lengths for indium diffusing from the upper and lower pyramids.<sup>12)</sup>

Indium diffusion is expected to occur during the epitaxial growth of quantum structures.<sup>34–36)</sup> Figure 13 shows the effect of indium diffusion on the position of the levels and their separation according to the model developed by us in a previous paper.<sup>12)</sup> The diffusion is assumed isotropic, namely the diffusion length is the same for both upper and lower pyramids and wetting layers. Even though indium diffusion smooths out the sharp edges of the InAs-GaAs interfaces, the levels move up as the diffusion length increases. This is because of

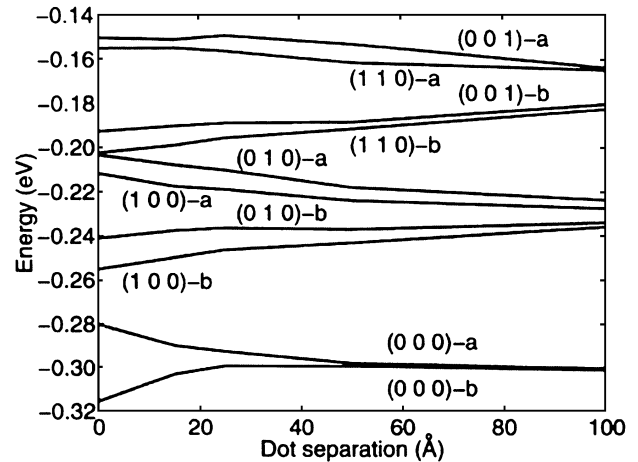


Fig. 12. Eigenenergies as a function of dot distance considering both the exact strain distribution and piezoelectricity. Indium diffusion was not considered.

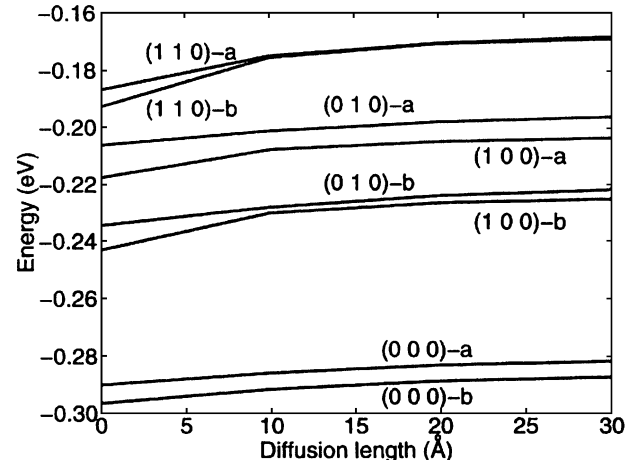


Fig. 13. Eigenenergies as a function of indium diffusion length for a constant dot separation of 25 Å.

indium conservation, implying that the indium that is added to the barrier comes from the pyramids and wetting layers. The result is a decrease of the pyramid size as more indium diffuses out (longer diffusion length in Fig. 13) pushing up the energy levels.

Another possibility concerning indium diffusion is anisotropic diffusion. In this case, the diffusion length is different for the cases of indium diffusing upwards and downwards. A consequence of this effect is the observation of an increase of dot size for dots belonging to the last grown layers.<sup>10,37)</sup> Most of the indium seems to come from detached pyramid tips, resulting in more rounded structures in the lower layers. Electronic coupling in this case occurs between non-identical structures. We modeled this effect by assuming isotropic diffusion with a diffusion length of 10 Å and removing the tip of the lower pyramid. Figure 14 shows the position of the levels as a function of the lower pyramid tip truncation length measured from the tip. A truncation length  $h_t$  means that up to  $h_t$  of the lower pyramid from its tip has been cut off, leaving a truncated pyramid with the same square base but a flat square top at a distance  $h - h_t$  from the base, where  $h$  is the original pyramid height. While changing the truncation

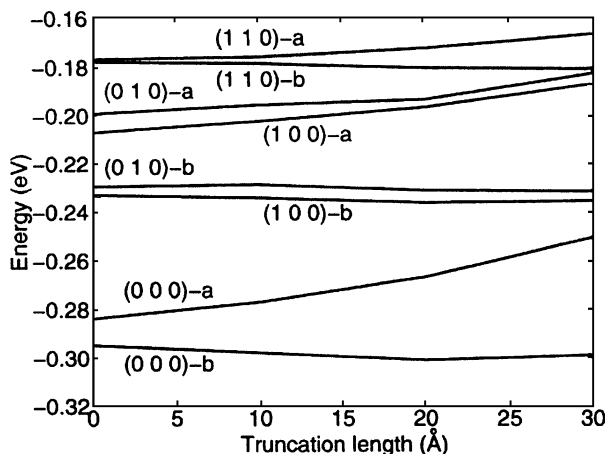


Fig. 14. Eigenenergies as a function of dot truncation length for a constant dot separation of 15 Å.

length, we keep the dot-dot separation  $h_{tb}$  constant at 15 Å. The level splitting is very large in this case for all levels in the dots, as shown in Fig. 14. This can be understood in terms of coupling between unequal structures: while the larger lobes of all bonding states are in the larger dot, the larger lobes of all antibonding states are in the smaller dot. Thus, as the diameter of the smaller dot decreases, the energies of the antibonding states increase leaving the energy of the bonding states almost constant.

### Acknowledgements

This work was supported by CRI from the University of Illinois and NSF Grants No. ECS 95-09751 and No. DMR 94-22496. We are indebted to S. Nagaraja for technical assistance.

- 1) S. Fafard, K. Hinzer, S. Raymond, M. Dion, J. McCaffrey, Y. Feng and S. Charbonneau: *Science* **274** (1996) 1350.
- 2) J. L. Jimenez, L. R. C. Fonseca, D. J. Brady, J. P. Leburton, D. E. Wohlfert and K. Y. Cheng: *Appl. Phys. Lett.* **71** (1997) 3558.
- 3) K. Imamura, Y. Sugiyama, Y. Nakata, S. Muto and N. Yokoyama: *Jpn. J. Appl. Phys.* **34** 1445 (1995) 3558.
- 4) S. Tarucha, D. G. Austing, T. Honda, R. J. van der Hage and L. P. Kouwenhoven: *Phys. Rev. Lett.* **77** (1996) 3613.
- 5) M. Fricke, A. Lorke, J. P. Kotthaus, G. Medeiros-Ribeiro and P. M. Petroff: *Europhys. Lett.* **36** (1996) 197.
- 6) G. S. Solomon, J. A. Trezza, A. F. Marshall and J. S. Harris, Jr.: *Phys.*

- 7) M. S. Miller, J. O. Malm, M. E. Pistol, S. Jeppesen, B. Kowalski, K. Georgsson and L. Samuelson: *J. Appl. Phys.* **80** (1996) 3360.
- 8) N. N. Ledentsov *et al.*: *Phys. Rev. B* **54** (1996) 8743.
- 9) L. R. C. Fonseca, J. L. Jimenez, J. P. Leburton and Richard M. Martin: *Phys. Rev. B* **57** (1998) 4017.
- 10) N. N. Ledentsov *et al.*: *Solid-State Electronics* (Elsevier, Great Britain, 1996) Vol. 40, Nos. 1–8, p. 785.
- 11) J. P. Perdew and Y. Wang: *Phys. Rev. B* **45** (1992) 13244.
- 12) L. R. C. Fonseca, J. L. Jimenez and J. P. Leburton: *Phys. Rev. B* **58** (1998) 9955.
- 13) J. Singh: *Physics of Semiconductors and Their Heterostructures* (McGraw-Hill, New York, 1993).
- 14) S. L. Chuang: *Physics of Optoelectronic Devices* (Wiley, New York, 1995).
- 15) M. Grundmann, O. Stier and D. Bimberg: *Phys. Rev. B* **52** (1995) 969.
- 16) J. L. Jimenez, L. R. C. Fonseca, J. P. Leburton and D. J. Brady: unpublished.
- 17) D. Jovanovic and J. P. Leburton: *Phys. Rev. B* **49** (1994) 10841.
- 18) R. G. Parr and W. Yang: *Density-Functional Theory of Atoms and Molecules* Oxford University Press, New York, 1989.
- 19) J. F. Janak: *Phys. Rev. B* **18** 7165 (1978) 10841.
- 20) J. C. Slater: *Adv. Quantum Chem.* **6** (1972) 1.
- 21) M. A. Cusack, P. R. Briddon and M. Jaros: *Phys. Rev. B* **54** (1996) 969 R2300.
- 22) T. Inui, Y. Tarabe and Y. Onodera: *Group Theory and its Applications in Physics* (Springer, New York, 1996).
- 23) J. M. Garcia, G. Medeiros-Ribeiro, K. Schmidt, T. Ngo, J. L. Feng, A. Lorke, J. Kotthaus and P. M. Petroff: *Appl. Phys. Lett.* **71** (1994) 2252.
- 24) We use Mulliken notation for the irreducible representations, as described in: T. Inui, Y. Tanabe and Y. Onodera: *Group Theory and its Applications in Physics* (Springer, Berlin, 1996).
- 25) J. Shumway, L. R. C. Fonseca, J. P. Leburton and D. Ceperley: unpublished.
- 26) S. Nagaraja, P. Matagne, V.-Y. Thean, J. P. Leburton, Y.-H. Kim and R. M. Martin: *Phys. Rev. B* **56** (1997) 15752.
- 27) I.-H. Lee, V. Rao, R. M. Martin and J. P. Leburton: *Phys. Rev. B* **56** (1998) 9035.
- 28) M. Macucci, K. Hess and G. J. Iafrate: *Phys. Rev. B* **55** (1997) R4879.
- 29) M. Koskinen, M. Manninen and S. M. Reimann: *Phys. Rev. Lett.* **79** (1997) 1389.
- 30) R. O. Jones: *Ab Initio Methods in Quantum Chemistry*, ed. K. P. Lawley (Wiley, New York, 1987) p. 413.
- 31) K. E. Schmidt and D. M. Ceperley: *Monte Carlo Methods in Condensed Matter Physics*, eds. K. Binder, Topics in Applied Physics, No. 71 (Springer, Heidelberg, 1992) p. 205.
- 32) G. D. Mahan: *Many-Particle Physics* (Plenum, New York, 1990).
- 33) R. J. Luyken, A. Lorke, M. Haslinger, B. T. Miller, M. Fricke, J. P. Kotthaus, G. Medeiros-Ribeiro and P. M. Petroff: unpublished.
- 34) K. Muraki, S. Fukatsu, Y. Shiraki and R. Ito: *Appl. Phys. Lett.* **61** (1992) 557.
- 35) U. Woggon, W. Langbein, J. M. Hvam, A. Rosenauer, T. Remmeli and D. Gerthsen: *Appl. Phys. Lett.* **71** (1997) 377.
- 36) N. Grandjean, J. Massies and O. Tottreau: *Phys. Rev. B* **55** (1997) R10 189.
- 37) W. Wu, J. R. Tucker, G. S. Solomon and J. S. Harris, Jr.: *Appl. Phys. Lett.* **71** (1997) 1083.